Journal of Materials Chemistry A

High Proton Conduction by Full Hydration in Highly Oxygen Deficient Perovskite

Journal:	*Journal of Materials Chemistry A*
Manuscript ID	TA-ART-03-2024-001978.R1
Article Type:	Paper
Date Submitted by the Author:	02-May-2024
Complete List of Authors:	Saito, Kei; Tokyo Institute of Technology, Chemistry Umeda, Kensei; Tokyo Institute of Technology, Chemistry Fujii, Kotaro; Tokyo Institute of Technology, Mori, Kazuhiro; High Energy Accelerator Research Organization Yashima, Masatomo; Tokyo Institute of Technology, Chemistry

ARTICLE

High Proton Conduction by Full Hydration in Highly Oxygen Deficient Perovskite

Received 00th January 20xx,
Accepted 00th January 20xx

DOI: 10.1039/x0xx00000x

Kei Saito,[a] Kensei Umeda,[a] Kotaro Fujii,[a] Kazuhiro Mori[b,c,d] and Masatomo Yashima*[a]

Abstract: Ceramic proton conductors are important in various applications such as fuel cells. In contrast to the conventional acceptor doping into the perovskite-type oxide without oxygen vacancies, donor doping into highly oxygen deficient perovskite is a novel strategy to achieve reduced proton trapping. Here, we report high proton conduction (e.g., 10 mS cm^{-1} at 235 °C) and chemical stability of highly oxygen deficient perovskite, W^{6+}-donor-doped $BaScO_{2.5}$ ($BaSc_{0.8}W_{0.2}O_{2.8}$). The high conductivity is attributed to both high proton concentration and proton diffusion coefficient *D*. The high *D* at low and intermediate temperatures is attributed to its low activation energy, suggesting reduced proton trapping. The high proton concentration is ascribed to both high oxygen deficiency in $BaSc_{0.8}W_{0.2}O_{2.8}$ and full hydration in hydrated $BaSc_{0.8}W_{0.2}O_{2.8}$ ($BaSc_{0.8}W_{0.2}O_{3.0}H_{0.4}$). A reason for the higher proton conductivity of $BaSc_{0.8}W_{0.2}O_{2.8}$ compared with $BaSc_{0.8}Mo_{0.2}O_{2.8}$ is higher fractional water uptake of $BaSc_{0.8}W_{0.2}O_{2.8}$, which is attributable to the large lattice volume of $BaSc_{0.8}W_{0.2}O_{2.8}$ due to the larger sized W cation than Mo cation. Present findings would open new avenues for clean energy societies.

Introduction

The need to improve energy efficiency has driven the development of fuel cell technology, of which solid oxide fuel cells (SOFCs) are a prime example.[1–9] Widespread applications of commercially available yttria stabilized zirconia (YSZ) electrolytes in SOFCs are limited by their high operating temperature (700–1000 °C). Since the activation energy for proton (H^+) conductivity is generally lower than that for oxide ion (O^{2-}) conductivity, it is known that H^+ conductors exhibit higher conductivity than O^{2-} conductors at low and intermediate temperatures (50–500 °C).[10–18] Therefore, as a technology alternative to the SOFCs, protonic ceramic fuel cells (PCFCs) have recently been attracting much attention.[10–12,19] Furthermore, there has been great interest in proton-conducting electrolysis cells (PCECs), because they can effectively convert electrical energy into chemical energy.[11,20–22] Proton conducting oxides used in PCFCs and PCECs have a lower operating temperature than oxide ion conductors in the SOFCs and solid oxide electrolysis cells (SOECs), enabling a stable energy supply at a lower cost. To develop high-performance PCFCs and PCECs, high proton conductivity of electrolytes is required. Thus, there is a need to search for proton conductors exhibiting high conductivities and high chemical stability at low and intermediate temperatures.

Many salt, hydrate, and polymer materials exhibit high proton conductivity, however, decompose at intermediate temperatures.[23–25] For example, CsH_2PO_4 shows high proton conduction from 230 to 254 °C, but decomposes above 254 °C.[23] In contrast, the oxides are generally chemically stable, but exhibit low proton conductivity at low and intermediate temperatures. Perovskite-type oxides such as $BaCeO_3$- and $BaZrO_3$-based materials are representative proton conductors.[17,26–35] A major problem of these conventional proton conductors is proton trapping, which results in low proton conductivity at low and intermediate temperatures.[18] The conventional method to improve the proton conductivity is acceptor M^{3+} doping into $Ba^{2+}B^{4+}O_3$ perovskite where M^{3+} is an acceptor with lower valence 3+ than 4+ of the host B^{4+} cation. Here, the acceptor is the dopant cation *M* with a lower valence than the host cation *B* and the δ is the amount of oxygen vacancies in $BaB_{1-x}M_xO_{3-\delta}$. Acceptor doping results in the formation of oxygen-deficient $BaB_{1-x}M_xO_{3-\delta}$ (e.g., *B* = Ce, and *M* = Y for $BaCe_{0.9}Y_{0.1}O_{2.95}$). Proton conduction is facilitated by hydration, forming the protons H^+ in $BaB_{1-x}M_xO_{3-\delta+y/2}H_y$ where *y* is proton concentration. However, the proton H^+ is trapped by the dopant cation M^{3+} with effective negative charge of −1 compared to the host B^{4+} cation via the electrostatic attraction. This proton trapping can result in proton-dopant cation association, higher apparent activation energy for proton conductivity and lower proton conduction at low and intermediate temperatures.[18] Therefore, if the proton trapping is reduced, high proton conductivity is expected at low and intermediate temperatures. Another major problem of the conventional $BaCeO_3$- and $BaZrO_3$-based proton conductors might be the low proton concentration *y* due to small amount

[a] Department of Chemistry, School of Science, Tokyo Institute of Technology, 2-12-1-W4-17, O-okayama, Meguro-ku, Tokyo, 152-8551, Japan.
[b] Institute of Materials Structure Science / J-PARC Center, High Energy Accelerator Research Organization (KEK), 203-1 Shirakata, Tokai, Ibaraki 319-1106, Japan.
[c] Graduate Institute for Advanced Studies, The Graduate University for Advanced Studies (SOKENDAI), 203-1 Shirakata, Tokai, Ibaraki 319-1106, Japan.
[d] Graduate School of Science and Engineering, Ibaraki University, 203-1 Shirakata, Tokai, Ibaraki 319-1106, Japan.
Electronic Supplementary Information (ESI) available: [details of any supplementary information available should be included here]. See DOI: 10.1039/x0xx00000x

of oxygen vacancies δ (e.g., y = 0.08 and δ = 0.05 in $BaCe_{0.9}Y_{0.1}O_{2.95}$), leading to low proton conductivity.

Recently, many oxides with "intrinsic oxygen vacancies" have attracted much attention due to high proton and oxide-ion conductivities.[6,13,18,36–50] Here, the "intrinsic oxygen vacancies" v are the oxygen vacancies in a parent material (e.g., v in high temperature cubic Bi_2O_3v).[51] For example, several hexagonal perovskite-related oxides such as Ba_2LuAlO_5 have two-dimensional intrinsically oxygen deficient layers and high proton conductivities.[13,41,43–47,50] Very recently, we have reported quite high proton conduction (over 10 mS cm^{-1} above 320 °C) and high chemical stability in the cubic perovskite-type $BaSc_{0.8}Mo_{0.2}O_{2.8}$.[18] The cubic $BaSc_{0.8}Mo_{0.2}O_{2.8}$ perovskite is stabilized by Mo^{6+} donor-doping into the parent material $BaScO_{2.5}$ with three-dimensionally disordered intrinsic oxygen vacancies v in $BaScO_{2.5}v_{0.5}$. Here the donor is the cation dopant with higher valence compared with the host cation (6+ of Mo^{6+} is higher than 3+ of host Sc^{3+}). In contrast to the conventional acceptor doping, the donor doping can reduce the proton trapping due to the electrostatic repulsion between the proton and the donor, which has a higher effective charge than the host cation.[18] The reduced proton trapping in donor-doped perovskites leads to the low activation energy for the proton diffusion coefficient and high proton conduction at low and intermediate temperatures. The thermogravimetric (TG) and neutron powder diffraction (ND) analyses indicated that the $BaSc_{0.8}Mo_{0.2}O_{2.8}$ is not fully hydrated. The full hydration in donor-doped perovskite with disordered intrinsic oxygen vacancies would yield higher proton conduction compared with $BaSc_{0.8}Mo_{0.2}O_{2.8}$. Here, we report high proton conductivity (e.g., 10 mS cm^{-1} at 235 °C) in the highly oxygen deficient perovskite, W^{6+}-donor-doped $BaScO_{2.5}$ ($BaSc_{0.8}W_{0.2}O_{3.0}H_{0.4}$). In this study, we have selected the chemical composition, because (i) donor-doped $BaScO_{2.5}$ exhibits high proton conduction, (ii) W^{6+} can be a donor as well as Mo^{6+}, and (iii) W-containing oxides such as $La_{28-x}W_{4+x}O_{54+\delta}$ exhibit significant proton conductivity.[52–54]

Methods

$BaSc_{0.8}W_{0.2}O_{2.8-y/2}(OH)_y$ (BSW) sample was prepared by the solid-state-reaction method. Raw materials $BaCO_3$ (Kojundo Chemical Laboratory Co., 99.95%), Sc_2O_3 (Shin-Etsu Chemical Co., 99.99%), and WO_3 (Kojundo Chemical Laboratory Co., 99.99%) were mixed and ground in an agate mortar for ~1 h as ethanol slurries and as dried powders. The powders thus obtained were calcined in static air at 900 °C for 12 h. The calcined powders were ground into fine powders in the agate mortar for ~1 h as ethanol slurries and as dried powders. The fine powders were uniaxially pressed into pellets at ~150 MPa and then sintered in static air at 1600 °C for 10 h on an alumina boat. The sintered products were crushed with a tungsten carbide crusher, ground with the agate mortar for ~1 h as ethanol slurries and as dried powders. The obtained samples were uniaxially pressed into pellets at ~150 MPa, isostatically pressed into pellets at ~200 MPa, and sintered in static air at 1600 °C for 10~20 h on the alumina boat. The relative densities of the sintered pellets of BSW were 70~74%. The sintered pellets of BSW were used for the impedance and direct current (DC) electrical conductivity measurements. Parts of the sintered pellets were crushed and ground into fine powders (as-prepared BSW powders) to carry out X-ray powder diffraction (XRD), X-ray fluorescence (XRF), inductively coupled plasma optical emission spectroscopy (ICP-OES), and TG measurements. The atomic ratio of the as-prepared BSW powders was determined to be Ba: Sc: W = 1.0: 0.8: 0.2 by XRF (NEX DE, Rigaku Co.) and ICP-OES analyses (SPS3500DD, Hitachi High-Tech Co.), which agreed with that of the nominal composition. Cu Ka XRD data of the as-prepared BSW powders were measured at 24 °C by a laboratory-based X-ray diffractometer (MiniFlex, Rigaku Co.). XRD data of the mixture of the as-prepared BSW powders and Si internal standard were also measured to investigate its lattice parameter. The lattice parameter of the as-prepared BSW powders was refined by Rietveld analyses of the XRD data using *Z-Rietveld*[55] software. Scanning electron microscope (SEM) observation of a sintered pellet of BSW was performed using a VE-8800 SEM microscope (Keyence Co.) (**Figure S1**).

Wet BSW powders for TG-MS, IR, and Raman scattering measurements were prepared as follows. The as-prepared BSW powders were heated to 1000 °C in dry air ($P(H_2O)$ < 1.5×10^{-4} atm) and kept for 1 h to remove water, and then the atmosphere was switched to H_2O-saturated air flow (water vapor partial pressure $P(H_2O)$ = 0.02 atm) at the same temperature 1000 °C. In cooling process, the sample was kept for 1 h at 1000, 900, 800, 700, 600, 500, 400, 300, 200, 100, and 25 °C to reach equilibrium. TG-MS analyses of the wet BSW powders were performed using RIGAKU Thermo Mass Photo under He flow at a heating rate of 20 °C min^{-1} up to 1000 °C. The proton concentration of BSW was investigated from 1000 to 100 °C by TG analysis (STA449 Jupiter, Netzsch Co.; **Figure S2**). The as-prepared BSW powders were first heated to 1000 °C in dry air ($P(H_2O)$ < 1.5×10^{-4} atm) and kept for 1 h to dehydrate. The gas subsequently switched to wet air ($P(H_2O)$ = 0.02 atm). In cooling process, the sample weight was recorded keeping the temperature at 1000, 950, 900, 850, 800, 750, 700, 650, 600, 550, 500, 450, 400, 350, 300, 250, 200, 150, 100 and 50 °C for 1 h to reach equilibrium. The proton concentration y in BSW was calculated from the weight increase assuming that the sample contains no protons (y = 0) at 1000 °C in dry air and that the weight increase was due to water incorporation only. The hydration enthalpy and entropy were estimated using the TG data (**Table S1** and **Figure S3**). Raman spectrum of the wet BSW powders was collected using NRS-4100 (JASCO Co.) with excitation wavelength of 532 nm. IR data for the wet BSW powders were measured using FT/IR-4200 (JASCO Co.).

Impedance spectra of the sintered pellet of BSW (4.7 mm in diameter, 11 mm in thickness) with Pt electrodes were recorded with a Solartron 1260 impedance analyzer in the frequency range from 0.1 Hz to 10 MHz with an applied alternating voltage of 100 mV in wet atmospheres (water vapor partial pressure $P(H_2O)$ = 0.02 atm) and dry conditions ($P(H_2O)$ < 1.5×10^{-4} atm) on cooling. Equivalent-circuit analysis was performed to extract the bulk and grain-boundary conductivities using *Zview*

software (Scribner Associates, Inc.). Oxygen partial pressure $P(O_2)$ dependencies of the DC electrical conductivity of the sintered pellet of BSW (4.7 mm in diameter and 11 mm in length) were investigated by a DC four-probe method with Pt electrodes using a mixture of O_2, air, N_2 and 5% H_2 in N_2 under wet conditions ($P(H_2O)$ = 0.02 atm) where the $P(O_2)$ was monitored with an oxygen sensor placed at the outlet of the apparatus. The isotope effect of the sintered pellet of BSW was evaluated by the DC electrical conductivity measurements in D_2O- and H_2O-saturated air (water vapor pressure = 0.02 atm).

Neutron diffraction experiments of wet pellets of BSW were performed at −243 °C with time-of-flight (TOF) neutron diffractometer SPICA at the MLF of the J-PARC.[56] The wet pellets of BSW for neutron diffraction measurements were prepared as follows. The sintered pellets of BSW were heated to 1000 °C in dry air ($P(H_2O) < 1.5\times10^{-4}$ atm) and kept for 1 h in order to remove water, and then the atmosphere was switched to D_2O-saturated air flow (water vapor pressure = 0.02 atm) at the same temperature 1000 °C. In cooling process, the sample was kept for 2 h at 1000, 900, 800, 700, 600, 500, 400, 300, 200, 100, and 25 °C to reach equilibrium. Rietveld analyses were performed with *Z-Rietveld*[55] using neutron diffraction data taken with the backscattering bank of the SPICA. Bond-valence based energy landscape (BVEL) for a test proton in BSW was calculated using refined crystal parameters at −243 °C with the *SoftBV* program.[57,58]

Static DFT calculations and *ab initio* molecular dynamics (AIMD) simulations were performed for the 3 × 3 × 3 supercell $Ba_{27}Sc_{22}W_5O_{81}H_{12}$ (~ $[BaSc_{0.8}W_{0.2}O_3H_{0.4}]_{27}$) using the Vienna ab initio simulation package (VASP)[59] code with the projector augmented wave (PAW) method and the Perdew–Burke–Ernzerhof (PBE) functional in the generalized gradient approximation (GGA). To reduce the computational cost, the reciprocal space integration was carried out only at the Γ point and the cut-off energy was set to 400 eV for all the calculations. First, we optimized the structures for 36 structural models of $Ba_{27}Sc_{22}W_5O_{81}$ with different Sc and W arrangements using the background charge. We optimized the structures of all the 8 structural models with only the W–W pairs longer than 5 Å. In addition, we optimized the structures of selected 28 structural models containing W–W pair(s) shorter than 5 Å. The total energies of the 8 structural models without W–W pairs shorter than 5 Å were significantly lower than those of the 28 structural models with W–W pair(s) shorter than 5 Å, which can be ascribed to the stronger repulsion between W^{6+} and W^{6+} cations compared with the repulsion between W^{6+} and Sc^{3+} cations. Then, the structural optimization of $Ba_{27}Sc_{22}W_5O_{81}H_{12}$ was performed based on the structural model of $Ba_{27}Sc_{22}W_5O_{81}$ with the lowest total energy. Here, the hydrogen atoms were put near selected oxygen atoms and the OH distance was set to about 1 Å in the initial structure of $Ba_{27}Sc_{22}W_5O_{81}H_{12}$. **Figure S4** shows the optimized structure of $Ba_{27}Sc_{22}W_5O_{81}H_{12}$, which was used as the initial structure of the AIMD simulations. The AIMD simulations were performed at a constant temperature 1500 °C with a time step of 0.5 fs within the canonical ensemble (NVT) using a Nosé thermostat, after the heating process (1 °C fs^{-1}) within the micro-canonical (NVE) ensemble. The AIMD snapshots and trajectories were visualized using the *OVITO* program.[60] The refined crystal structure, BVEL, and the probability density distribution of H atoms from the AIMD simulations were drawn with *VESTA 3*.[61]

Results and Discussion

A white sample of cubic perovskite-type $BaSc_{0.8}W_{0.2}O_{2.8-y/2}(OH)_y$ (= $BaSc_{0.8}W_{0.2}O_{2.8}\cdot(y/2)\ H_2O$ = BSW) was successfully synthesized via the solid-state reaction (Methods and **Figure S5** in the Supporting Information). The formation of the cubic perovskite phase of BSW is reasonable, because its tolerance factor is close to unity (1.006). To show proton conduction, we carried out H/D isotope exchange experiments on BSW at 250 °C in D_2O-saturated and H_2O-saturated air. Direct current (DC) electrical conductivity σ_{DC} of BSW was measured by the DC four-probe method, and exhibited a decrease from $\sigma_{DC}(H_2O)$ to $\sigma_{DC}(D_2O)$, as the atmosphere was changed from H_2O-saturated air to D_2O-saturated air (**Figure S6**). Here, the $\sigma_{DC}(H_2O)$ and $\sigma_{DC}(D_2O)$ represent the DC electrical conductivity in H_2O- and D_2O-saturated air, respectively. The $\sigma_{DC}(H_2O)/\sigma_{DC}(D_2O)$ ratio was close to the value (1.41) from the classical theory.[62] The σ_{DC} was almost independent of the oxygen partial pressure $P(O_2)$ in the wide $P(O_2)$ range between 10^{-20} and 1 atm at 300 and 100 °C under wet conditions (water vapor partial pressure = 0.02 atm), indicating the high chemical and electrical stability, and suggesting ionic conduction and no significant electronic and hole conduction (**Figure 1a**). The electrical conductivity of BSW in wet air σ_{wet} was much higher than that in dry air σ_{dry} (**Figure S7a**; e.g., σ_{wet} = 55 σ_{dry} at 193 °C), indicating the transport number $(\sigma_{wet} - \sigma_{dry})/\sigma_{wet}$ close to unity (**Figure S7b**). These results show that protons are the dominant conducting species in BSW.

To examine the proton conductivity σ_b in bulk BSW, we performed impedance measurements (**Figures 1b,c and S8–S11, Table S2**). Typical impedance spectra of BSW are shown in **Figures 1b** and **S9a**, indicating two semicircles due to the bulk and grain-boundary (gb) responses. To determine the bulk and gb conductivities, we performed equivalent circuit analyses employing the models shown in **Figure S10**. We obtained reasonable fitting results (**Figures 1b** and **S9**), capacitance values (**Table S2**), and KK residuals (**Figure S8, Supplementary Note 1** in ESI). BSW exhibited higher σ_b than the gb conductivity (**Figure S11**). It should be noted that BSW showed high σ_b in wet air within the "Norby gap"[63] (e.g., 10 mS cm^{-1} at 235 °C) and higher σ_b compared with other proton conductors[18,64–70] (**Figure 1c**). BSW exhibited 10 times higher σ_b than that of $BaZr_{0.8}Y_{0.2}O_{2.9-y/2}(OH)_y$ (BZY; Ref. [64]), 73 times higher σ_b than that of $BaCe_{0.9}Y_{0.1}O_{2.95-y/2}(OH)_y$ (BCY; Ref. [30]), and 3.6 times higher σ_b than that of BSM (Ref. [18]) at 235 °C. The higher σ_b of BSW compared with BZY, BCY, and BSM is attributable to the higher proton concentration y in $BaB_{1-x}M_xO_{3-\delta-y/2}(OH)_y$ and the higher proton diffusion coefficient D, as discussed below. The σ_b of BSW was 6.8 times higher than that of $BaZr_{0.4}Sc_{0.6}O_{2.7-y/2}(OH)_y$ (BZS; Ref. [65]) at 137 °C, which can be attributed to the higher D of BSW, as indicated below. Therefore, it is noteworthy that

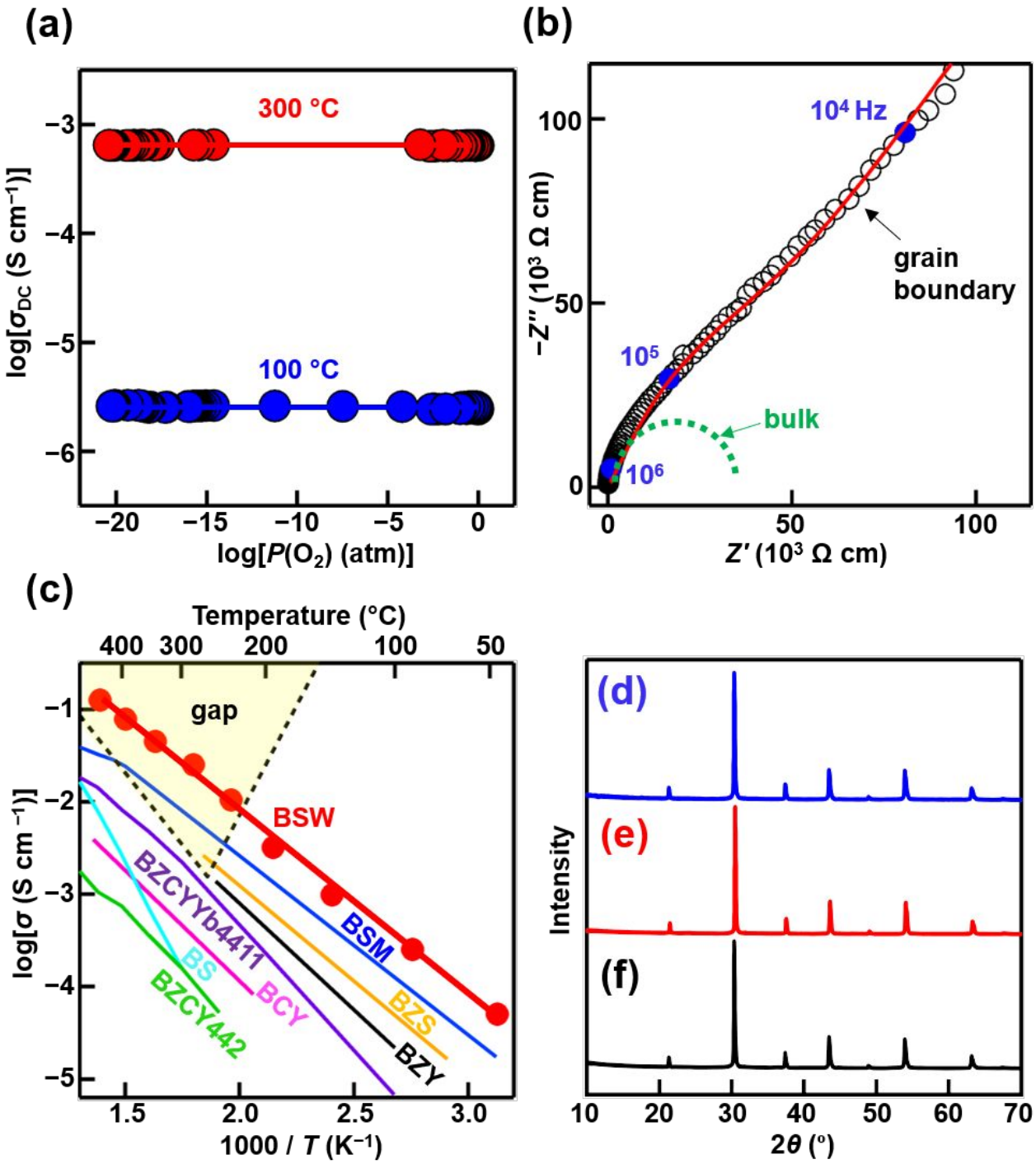

Figure 1. High proton conductivity, high electrical and chemical stability, and high chemical stability of BSW. (a) Oxygen partial pressure dependencies of the DC electrical conductivity σ_{DC} for BSW at 300 °C (red closed circles and solid line) and 100 °C (blue closed circles and solid line) under wet conditions. (b) Complex impedance plots of BSW at 46 °C recorded in wet air. The number of each blue closed circle denotes the frequency. The red solid line represents the fitting curve, which indicates a semicircle due to bulk response and a part of semicircle due to grain-boundary response. The green dotted, high-frequency semicircle represents the bulk resistance. (c) Norby gap[63] and Arrhenius plots of total AC conductivity of $BaScO_2(OH)$ (BS)[68] and $BaZr_{0.4}Ce_{0.4}Y_{0.2}O_{2.9-y/2}(OH)_y$ (BZCY442)[69] and bulk conductivity of BSW, $BaSc_{0.8}Mo_{0.2}O_{2.8-y/2}(OH)_y$ (BSM),[18] $BaZr_{0.4}Sc_{0.6}O_{2.7-y/2}(OH)_y$ (BZS),[65] $BaZr_{0.8}Y_{0.2}O_{2.9-y/2}(OH)_y$ (BZY),[64] and $BaCe_{0.9}Y_{0.1}O_{2.95-y/2}(OH)_y$ (BCY),[30] and $BaZr_{0.4}Ce_{0.4}Y_{0.1}Yb_{0.1}O_{2.9-y/2}(OH)_y$ (BZCYYb4411)[70] in wet atmospheres. XRD patterns of BSW after annealing at 250 °C for 240 h under (d) CO_2 and (e) 5% H_2 in N_2 and (f) before the annealing.

BSW exhibits higher σ_b compared with the best ceramic proton conductors.

Electrochemical devices such as PCFCs require high chemical stability of proton-conducting electrolytes for long-term use. For the investigation of the chemical stability in CO_2,

BSW powders were annealed under CO_2 flow at 250 °C for 240 h. Between the X-ray powder diffraction (XRD) patterns before and after annealing, no significant difference was observed, indicating the high chemical stability of BSW against CO_2 (**Figure 1d,f**). High chemical stability of BSW was also confirmed in 5% H_2 in N_2 at 250 °C for 240 h, in H_2 at 450 °C for 100 h, in CO_2 at 450 °C for 200 h, and in static air at room temperature for 100 h (**Figures 1e,f** and **S12**). No significant difference was observed between the XRD patterns before and after the impedance measurements in dry and wet air (three heating and cooling cycles), indicating also the high chemical stability of BSW (**Figure S13**). Furthermore, the stability of the electrical conductivity of BSW in wet H_2, wet air, and wet CO_2 was investigated. There was no significant change of the electrical conductivity, indicating high conductivity stability of BSW (**Figure S14**). These high chemical stabilities, high proton transport number (**Figure S7b**), high chemical and electrical stability (**Figure 1a**), and high proton conductivity (**Figure 1c**) indicate that BSW is a superior proton conductor.

Next, we delve into the reasons for the high bulk proton conductivity σ_b of BSW. The σ_b is proportional to the proton concentration y and proton diffusion coefficient D in bulk $BaSc_{0.8}W_{0.2}O_{2.8-y/2}(OH)_y$ (BSW): $\sigma_b \propto y \times D$. To examine the y and hydration of BSW, thermogravimetric-mass spectrometric (TG-MS) and TG measurements were performed. The TG-MS results of wet BSW powders showed that dehydration was the primary cause of the weight loss upon heating (**Figure S15**). Therefore, the y could be estimated from the weight change in TG curve. The TG data showed the typical behavior of hydration with higher proton concentration y at lower temperatures (**Figures 2a** and **S2**). The proton concentrations y of BSW (e.g., y = 0.40 at 100 °C and y = 0.36 at 400 °C) were higher than those of BSM (e.g., y = 0.32 at 100 °C),[18] BCY (e.g., y = 0.08 at 100 °C),[30] and BZY (e.g., y = 0.17 at 400 °C)[66] (**Figure 2a**). The higher y in BSW is a reason for its higher proton conductivity compared to BSM, BCY, and BZY. The y in hydrated perovskite $BaB_{1-x}M_xO_{3-\delta-y/2}(OH)_y$ increases with increasing the amount of oxygen vacancies δ in $BaB_{1-x}M_xO_{3-\delta}$ without water (**Figure 2b**). Thus, the higher y in BSW can be due to higher oxygen deficiency δ = 0.2 in BSW without water compared with BCY (δ = 0.05) and BZY (δ = 0.1). These results indicate that one reason for the high proton conductivity in BSW is the high oxygen deficiency δ = 0.2 in BSW without water.

To examine the hydration and proton concentration of bulk BSW, we performed the Rietveld analyses of neutron diffraction (ND) data of hydrated (deuterated) BSW (= $BaSc_{0.8}W_{0.2}O_{2.8-y/2}(OD)_y$ = $BaSc_{0.8}W_{0.2}O_{2.8}\cdot(y/2)\ D_2O$) at −243 °C. The calculated intensities based on the cubic $Pm\bar{3}m$ perovskite-type structure were in good agreement with the observed ones (**Figures 2c**, **2d, and 2e**), giving reasonably small reliability factors (R_{wp} = 5.08%, R_B = 2.84%, R_F = 3.32%; **Table 1**). The refined lattice parameter of BSW (4.153511(13) Å) was in agreement with that optimized by the DFT calculations (4.18 Å). The refined atomic coordinates of D atom in BSW were in agreement with those of $BaSc_{0.8}Mo_{0.2}O_{2.8-y/2}(OD)_y$ (Ref. [18]) and optimized by the DFT calculations (**Table S3**, **Figure S4**). The OD bond length calculated for the refined structure of BSW (1.03(3) Å) agreed with the OH bond length values estimated from the infrared (IR) spectroscopy data of wet BSW powders (1.00 Å; **Figure S16a**) and Raman scattering data of wet BSW powders (0.99 Å; **Figure S16b**) and from the optimized structure by DFT calculations (0.99 Å; **Figure S4**) within two estimated standard deviations. These results indicate the formation of hydroxide ions OH in $BaSc_{0.8}W_{0.2}O_{2.8-y/2}(OH)_y$ and OD in $BaSc_{0.8}W_{0.2}O_{2.8-y/2}(OD)_y$. The bond-valence sums (BVSs) for Ba atom (2.1) and O atom (2.1) were in good agreement with their formal charges (**Table 1**). The average BVS of the cations at Sc/W site (3.2) was consistent with the average oxidation number (3.6). The BVS (0.8) for defective D atom was also consistent with its formal charge. These results indicate the validity of the refined crystal structure of BSW (**Figure 2e**). It should be noted that the occupancy factor of O atom was 1.000(4), indicating the full hydration where the O site was fully occupied by O atoms. Furthermore, the proton (deuteron) concentration y calculated from the refined occupancy factor of D atom y = 0.40(2) in bulk $BaSc_{0.8}W_{0.2}D_yO_{2.8+y/2}$ agreed with the value obtained from TG data y = 0.40. Therefore, these structural and TG analyses indicated that the chemical formula of bulk BSW was $BaSc_{0.8}W_{0.2}O_{3.000(12)}D_{0.40(2)}$ and water D_2O was fully incorporated as OD hydroxide ions in bulk BSW. Here, we define the fractional water uptake F_w as follows:

$$F_w = y/2\delta \quad (1)$$

where y and δ are the proton concentration and the amount of oxygen vacancies, respectively, in $BaB_{1-x}M_xO_{3-\delta-y/2}(OH)_y$. The F_w of BSW (1.00) was higher than those of leading proton conductors (**Table S4**). The F_w of $BaSc_{1-x}M_xO_{3-\delta}$ (M = Mo, W) increased with increasing the experimental lattice volume (**Figure S17a**). Therefore, the higher F_w of BSW (1.00) than that of BSM (0.8) can be attributed to the larger lattice volume of BSW compared with BSM due to larger ionic radius of W^{6+} cation compared with Mo^{6+} (**Figure S17**; See the **Supplementary Note 2** in ESI). Using Eq. (1), the proton concentration y can be expressed as $y = 2F_w\delta$, thus, y increases with increasing F_w and δ. Both F_w and δ of BSW are high and $y = 2F_w\delta$ of BSW is higher than those of other proton conductors $BaB_{1-x}M_xO_{3-\delta-y/2}(OH)_y$ (**Figure 2f**), leading to high proton conductivity. The BSM is not fully hydrated, while the BSW is fully hydrated due to its larger lattice volume compared with BSM, which would be a reason for higher proton conductivity of BSW compared with BSM.

Table 1. Results of refined crystal parameters and reliability factors in Rietveld analysis of the ND data of $BaSc_{0.8}W_{0.2}O_{2.600(12)}(OD)_{0.40(2)}$ (= $BaSc_{0.8}W_{0.2}O_{2.8}$ 0.200(12) D_2O = $BaSc_{0.8}W_{0.2}O_{3.000(12)}D_{0.40(2)}$) at −243 °C.

Site, atom label *X*	atom *Y*	*g*[a]	Wyckoff position	*x*	*y*	*z*	U_{iso} or U_{eq} (Å^2)[b]	BVS[c]
Ba	Ba	1[d]	1*b*	1/2	1/2	1/2	0.00881(16)	2.1
Sc/W	Sc	0.8[d]	1*a*	0	0	0	0.00881(12)	3.2
Sc/W	W	0.2[d]	1*a*	0	0	0	0.00881(12)	
O	O	1.000(4)	3*d*	1/2	0	0	0.00992(15)	2.1
D	D	0.0166(10)	24*m*	0.449(6)	0.248(6)	0	0.062(6)	0.8

Crystal system: cubic, Space group: $Pm\bar{3}m$, R_{wp} = 5.08%, R_B = 2.84%, R_F = 3.32%, Lattice parameter: *a* = 4.153511(13) Å.

[a] Occupancy factor of *Y* atom at the *X* site. *x*, *y*, and *z*: atomic coordinates.

[b] $U_{iso} = U_{iso}(Y; X)$: Isotropic atomic displacement parameter of *Y* atom at the *X* site, U_{eq}: Equivalent isotropic atomic displacement parameter of *Y* atom at the *X* site. Linear constraints in the Rietveld analysis: U_{iso}(Sc; Sc/W) = U_{iso}(W; Sc/W). U_{11}(O; O) = 0.01000(4) Å^2, U_{22}(O; O) = U_{33}(O; O) = 0.00989(17) Å^2. Here, $U_{ij}(Y; X)$: Anisotropic atomic displacement parameter of *Y* atom at the *X* site.

[c] BVS: Bond valence sum. Here, the bond-valence parameters (Ref. [71]) were used for the calculation of BVSs for Ba, O, and Sc/W. The bond-valence parameter of D atom in Ref. [72] was used for the calculation of BVS.

[d] Since the refined occupancy factors of Ba, Sc and W atoms agreed with 1, 0.8 and 0.2, respectively, within three standard deviations in preliminary analyses, they were fixed to these values.

ARTICLE

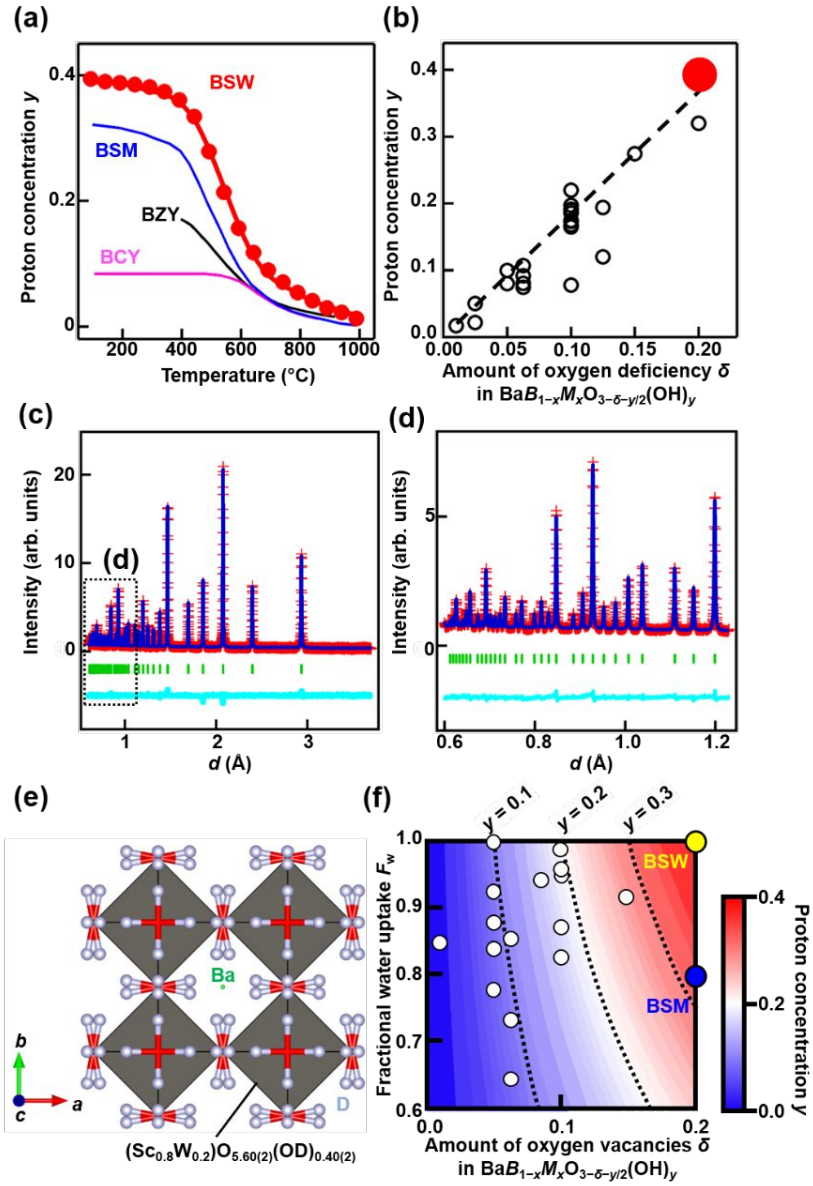

Figure 2. High proton concentration *y* in bulk BSW evidenced by TG and ND analyses. (a) Temperature dependencies of proton concentration *y* in $BaB_{1-x}M_xO_{3-\delta-y/2}(OH)_y$ (red circles and curve: BSW of this work. black curve: BZY.[66] pink curve: BCY.[30] blue curve: BSM.[18]), which were obtained by TG measurements. (b) Correlation between the amount of oxygen vacancies δ and *y* in $BaB_{1-x}M_xO_{3-\delta-y/2}(OH)_y$.[18,30,73,74] Red closed circle stands for the BSW data. (c,d) Rietveld patterns of ND data of BSW in the *d* ranges of (c) 0.60–3.70 Å and (d) 0.60–1.23 Å, which were taken at −243 °C. Blue lines and red crosses are calculated and observed intensities, respectively. Green tick marks denote calculated Bragg peak positions of cubic $Pm\bar{3}m$ BSW. The light blue line is the difference pattern. (e) Refined crystal structure of BSW, which was represented using $(Sc_{0.8}W_{0.2})O_{5.60(2)}(OD)_{0.40(2)}$ octahedra. Ba, O, and D atoms are denoted by the green, red, and gray spheres, respectively. The red/gray lines denote the OD bonds. The isotropic displacement spheres of Ba, O, and D atoms are plotted at the 10% probability level. (f) Plot of δ vs fractional water uptake F_w of BSW (yellow closed circle), BSM (blue closed circle), and other proton conductors (white closed circles).[18,30,73,74] Each dot line in panel (f) represents the inverse proportional relationship between F_w and δ ($F_w = y/2\delta$) for a constant proton concentration *y* in $BaB_{1-x}M_xO_{3-\delta-y/2}(OH)_y$ (y = 0.1, 0.2, and 0.3).

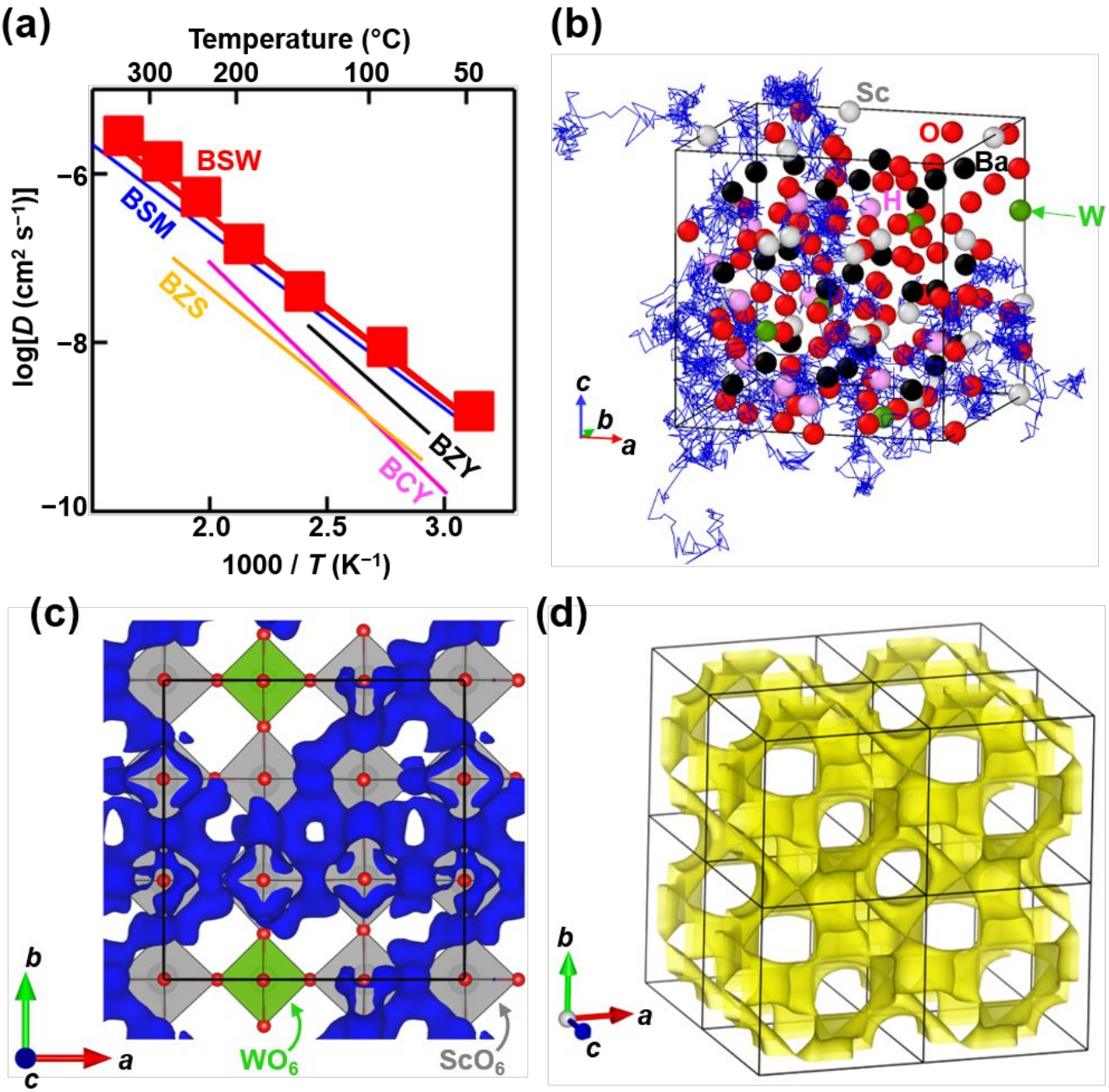

Figure 3. High proton diffusion coefficient of BSW and its structural origins. (a) Arrhenius plots of experimental bulk proton diffusion coefficient *D* of BSW (red circles and line), BSM (blue line),[18] BZS (yellow line),[65] BZY (black line),[66] and BCY (pink line),[67] which were estimated using bulk conductivity data and Eq. (2). (b) Blue trajectories of hydrogen atoms in $Ba_{27}Sc_{22}W_5O_{81}H_{12}$ (~ $[BaSc_{0.8}W_{0.2}O_3H_{0.4}]_{27}$) from AIMD simulations at 1500 °C. (c) Blue isosurface of the proton probability density at 0.001 Å^{-3} in the $Ba_{27}Sc_{22}W_5O_{81}H_{12}$ viewed along the *c* axis from the AIMD simulations at 1500 °C ($-0.2 \le x \le 1.2$; $-0.2 \le y \le 1.2$; $0.45 \le z \le 0.85$). The red, green, and gray spheres represent O, W, and Sc atoms, respectively. The green and gray squares denote WO_6 and ScO_6 octahedra, respectively. (d) Bond-valence based energy landscape (BVEL) for a test proton with the yellow isosurface at 0.43 eV, which was calculated for the crystal parameters refined using the ND data of BSW. Energy barrier for proton migration was estimated to be 0.41 eV from the BVEL, which agreed with the experimental activation energy for bulk diffusion coefficient 0.430(10) eV within two standard deviations. Black lines in panels (b) and (c) stand for the 3×3×3 supercell and the black lines in panel (d) denote the unit cells.

Next, we investigate high bulk proton diffusion coefficient *D* of BSW. The experimental *D* was estimated using the Nernst-Einstein equation

$$D = \sigma_b RT/F^2 y \quad (2)$$

where σ_b is the bulk conductivity, *R* is the gas constant, *T* is the absolute temperature, *F* is the Faraday constant, and *y* is the proton concentration obtained from the TG measurements. The *D* of BSW was higher than those of BZS, BZY, and BCY (**Figure 3a**). *Ab initio* molecular dynamics (AIMD) simulations supported the high *D* in BSW (**Figure S18**). From Eq. (2), the bulk conductivity σ_b can be expressed as $\sigma_b = DF^2y/RT$. Since both *D* and *y* of BSW are high (**Figures 2a,b,f** and **3a**), the σ_b of BSW is higher than σ_b of other proton conductors.

Next, we discuss the origins of high D of BSW. The activation energy E_a for D of the present W^{6+}-donor-doped $BaScO_{2.5}$ (BSW) was estimated to be 0.430(10) eV, which was close to that of the Mo^{6+}-donor-doped $BaScO_{2.5}$ (BSM) (0.41 eV)[18] and lower than those of the acceptor-doped proton conducting oxides such as BZY (0.48 eV),[66] BZS (0.47 eV),[65] $BaZr_{0.8}Sc_{0.2}O_{2.9-y/2}(OH)_y$ (0.50 eV),[65] and BCY (0.54 eV)[67] at low temperatures (50−170 °C). The low E_a of BSW suggests the reduced proton trapping, due to the repulsion between the donor and proton. To show the repulsion between the W^{6+} donor and protons, the trajectory and probability density distribution of protons in $Ba_{27}Sc_{22}W_5O_{81}H_{12}$ (~ $[BaSc_{0.8}W_{0.2}O_3H_{0.4}]_{27}$) were investigated using the AIMD simulations (**Figure 3b,c**), which indicates the long-range proton migration. It is noteworthy that most of protons are not near the oxide ions coordinated to a W and a Sc cation but to two Sc cations, indicating that the protons migrate around the ScO_6 octahedra while avoiding the WO_6 octahedra (**Figure 3b,c**). This result clearly indicates the repulsion between the W^{6+} donor and protons, supporting the reduced proton trapping. Since the protons migrate around ScO_6 octahedra, higher Sc concentration $1-x$ in $BaSc_{1-x}M_xO_{3-\delta-y/2}(OH)_y$ might be benefit for the high proton diffusivity. The Sc concentration in BSW (0.8) is higher than that in $BaSc_{0.6}Zr_{0.4}O_{3-\delta}$ (BZS: 0.6), which would be a reason for the higher D of BSW compared with BZS (BZS in **Figure 3a**). Also for BSM, the AIMD simulations showed similar Mo^{6+} donor-proton repulsion and proton migration around ScO_6 octahedra.[18]

It is interesting to point out that the trajectory from AIMD simulations shows the three-dimensional (3D) proton diffusion (**Figure 3b**), which was supported also by the bond-valence based energy landscape (BVEL) obtained for the refined crystal structure of BSW (**Figure 3d**). In contrast to Ba_2ScAlO_5 (Ref. [46]), Ba_2LuAlO_5 (Ref. [50]), and $BaY_{1/3}Ga_{2/3}O_{2.5}$ (Refs. [48,49]) with the ordered oxygen vacancies, the cubic perovskite-type BSW without water exhibits the occupational disorder of oxygen vacancies, which results in the 3D network of oxygen atoms and 3D proton diffusion in hydrated BSW. The 3D proton diffusion might be beneficial for the polycrystalline electrolytes in electrochemical devices.

Conclusions

In conclusion, we have demonstrated high proton conductivity (over 0.01 S cm^{-1} above 235 °C) in the novel material, cubic perovskite-type BSW (= $BaSc_{0.8}W_{0.2}O_{2.8-y/2}(OH)_y$ = $BaSc_{0.8}W_{0.2}O_{2.8+y/2}H_y$ = $BaSc_{0.8}W_{0.2}O_{2.8}\cdot(y/2)\ H_2O$) stabilized by W^{6+} donor-doping into $BaScO_{2.5}$ with disordered intrinsic oxygen vacancies. BSW exhibits high chemical stability under CO_2 H_2, and 5% H_2 in N_2 atmospheres at high temperatures and in ambient atmosphere at room temperature. The high bulk proton conductivity of BSW is attributable to its high concentration y and diffusion coefficient of protons. The high proton concentration is ascribed to both large amount of oxygen vacancies $\delta = 0.2$ in BSW without water ($BaSc_{0.8}W_{0.2}O_{3-d}$) and the full hydration in hydrated BSW (δ = 0.00 in $BaSc_{0.8}W_{0.2}O_{3-\delta}H_y$ = $BaSc_{0.8}W_{0.2}O_{3.0}H_{0.4}$). The BSM is not fully hydrated, but in BSW, which can be ascribed to the larger sized W^{6+} compared with Mo^{6+}. Since the proton hopping occurs between oxygen atoms, the presence of oxygen vacancies would lower the proton conductivity. Therefore, the full hydration in BSW enhances the proton conduction. The high proton diffusion coefficient D at low and intermediate temperatures is attributed to the low activation energy for D (0.43 eV), which suggests the reduced proton trapping due to the repulsion between the W^{6+} donor dopant and protons. The repulsion was indicated by the probability density distribution and trajectory of protons obtained in the AIMD simulations. High D was supported by the AIMD simulations. The high Sc concentration in BSW (0.8) can also be a reason for the high proton diffusion coefficient. “Stabilization of the perovskite with disordered intrinsic oxygen vacancies and full hydration by large-sized donor doping” would be an effective strategy towards next generation proton conductors.

Author Contributions

K. Saito and M. Y. designed research project. K. U. prepared the samples, carried out the XRD measurements and experiments of transport properties, and measured TG data. K. Saito analyzed the crystal structure and performed BVEL calculations. K. F. performed DFT calculations. K. M. and K. F. measured neutron diffraction data. Original manuscript was written and edited by K. Saito, K. U., K. F., and M.Y. M.Y. conceived the project and supervised the research. Funding acquisition and supervision: M. Y. and K. F. All authors participated in the data analysis, discussed the results, and read the manuscript. K. Saito and K. Umeda contributed equally to this work.

Conflicts of interest

There are no conflicts to declare.

Acknowledgements

We thank Mr. K. Matsuzaki and Mr. N. Ueno for their help with experiments and valuable discussions. We thank Shin-Etsu Chemical Co., Ltd. for arranging the chemical analyses and providing raw materials. We also acknowledge Kojundo Chemical Laboratory Co., Ltd. for providing raw materials. We especially thank to Ms K. Suda of the Materials Analysis Division, Open Facility Center, Tokyo Institute of Technology for the TG-MS measurements. We also thank Prof. S. Ito and Dr. M. Tada for performing IR and Raman measurements, respectively. We performed ND measurements by the project approval (JRR-3 Proposal Nos. 23627, 23623, 23613, 22614, 22610, and 22603; J-PARC: Proposal Nos. 2020L0804, 2020L0802, 2020L0801). Synchrotron X-ray diffraction experiments were performed by the project approval (SPring-8: 2023B2100, 2023A1684, 2022B0569, 2022B1195, and 2022A1270; PF: 2023G514, 2022G554, 2021G615, and 2021G549). K.S. acknowledges support from a JSPS Fellowship for Young Scientists, DC1 (23KJ0953). This work was supported by Adopting Sustainable

Partnerships for Innovative Research Ecosystem (ASPIRE) from the Japan Science and Technology Agency (JST) Grant No. JPMJAP2308, Adaptable and Seamless Technology Transfer Program through Target-driven R&D (A-STEP) from the JST Grant No. JPMJTR22TC, Grant-in-Aid for Scientific Research (KAKENHI, JP21K18182, JP22H04504, JP23K04887, JP23H04618, and JP240041) from the Ministry of Education, Culture, Sports, Science, and Technology of Japan, and JSPS Core-to-Core Program, Mixed Anion Research for Energy Conversion [JPJSCCA20200004]), and the Institute for Solid State Physics, the University of Tokyo.

References

1 J. B. Goodenough, *Nature*, 2000, **404**, 821.
2 B. C. H. Steele, A. Heinzel, *Nature*, 2001, **414**, 345.
3 E. Kendrick, J. Kendrick, K. S. Knight, M. S. Islam, P. R. Slater, *Nat. Mater.*, 2007, **6**, 871.
4 S. J. Skinner, J. A. Kilner, *Solid State Ion.*, 2000, **135**, 709.
5 T. Ishihara, H. Matsuda, Y. Takita, *J. Am. Chem. Soc.*, 1994, **116**, 3801.
6 M. Yashima, T. Tsujiguchi, Y. Sakuda, Y. Yasui, Y. Zhou, K. Fujii, S. Torii, T. Kamiyama, S. J. Skinner, *Nat. Commun.*, 2021, **12**, 556.
7 W. Zhang, K. Fujii, E. Niwa, M. Hagihala, T. Kamiyama, M. Yashima, *Nat. Commun.*, 2020, **11**, 1224.
8 H. Yaguchi, D. Morikawa, T. Saito, K. Tsuda, M. Yashima, *Adv. Funct. Mater.*, 2023, **33**, 2214082.
9 N. Tarasova, I. Animitsa, *Solid State Ion.*, 2018, **317**, 21.
10 T. Norby, *Nature*, 2001, **410**, 877.
11 W. Bian, W. Wu, B. Wang, W. Tang, M. Zhou, C. Jin, H. Ding, W. Fan, Y. Dong, J. Li, D. Ding, *Nature*, 2022, **604**, 479.
12 K. Jiao, J. Xuan, Q. Du, Z. Bao, B. Xie, B. Wang, Y. Zhao, L. Fan, H. Wang, Z. Hou, S. Huo, N. P. Brandon, Y. Yin, M. D. Guiver, *Nature*, 2021, **595**, 361.
13 S. Fop, K. S. McCombie, E. J. Wildman, J. M. S. Skakle, J. T. S. Irvine, P. A. Connor, C. Savaniu, C. Ritter, A. C. Mclaughlin, *Nat. Mater.*, 2020, **19**, 752.
14 C. Xia, Y. Mi, B. Wang, B. Lin, G. Chen, B. Zhu, *Nat. Commun.*, 2019, **10**, 1707.
15 C. Duan, J. Huang, N. Sullivan, R. O'Hayre, *Appl. Phys. Rev.*, 2020, **7**, 011314.
16 S. Choi, C. J. Kucharczyk, Y. Liang, X. Zhang, I. Takeuchi, H. Il Ji, S. M. Haile, *Nat. Energy*, 2018, **3**, 202.
17 T. Chen, Y. Jing, L. O. Anderson, K. Leonard, H. Matsumoto, N. Aluru, N. H. Perry, *J. Phys. Chem. C*, 2021, **125**, 26216.
18 K. Saito, M. Yashima, *Nat. Commun.*, 2023, **14**, 7466.
19 N. Tarasova, A. Galisheva, I. Animitsa, *Int. J. Hydrogen Energy*, 2021, **46**, 16868.
20 H. Ding, W. Wu, C. Jiang, Y. Ding, W. Bian, B. Hu, P. Singh, C. J. Orme, L. Wang, Y. Zhang, D. Ding, *Nat. Commun.*, 2020, **11**, 1907.
21 K. Leonard, Y. Okuyama, Y. Takamura, Y. S. Lee, K. Miyazaki, M. E. Ivanova, W. A. Meulenberg, H. Matsumoto, *J. Mater. Chem. A*, 2018, **6**, 19113.
22 D. Huan, W. Wang, Y. Xie, N. Shi, Y. Wan, C. Xia, R. Peng, Y. Lu, *J. Mater. Chem. A*, 2018, **6**, 18508.
23 S. M. Haile, C. R. I. Chisholm, K. Sasaki, D. A. Boysen, T. Uda, *Faraday Discuss.*, 2007, **134**, 17.
24 M. Nagao, T. Kamiya, P. Heo, A. Tomita, T. Hibino, M. Sano, *J. Electrochem. Soc.*, 2006, **153**, A1604.
25 S. R. Phadke, C. R. Bowers, E. D. Wachsman, J. C. Nino, *Solid State Ion.*, 2011, **183**, 26.
26 P. A. Stuart, T. Unno, J. A. Kilner, S. J. Skinner, *Solid State Ion.*, 2008, **179**, 1120.
27 I. Kosacki, H. L. Tuller, *Solid State Ion.*, 1995, **80**, 223.
28 H. Iwahara, T. Yajima, T. Hibino, K. Ozaki, H. Suzuki, *Solid State Ion.*, 1993, **61**, 65.
29 H. Iwahara, *Solid State Ion.*, 1996, **86–88**, 9.
30 K. D. Kreuer, *Annu. Rev. Mater. Res.*, 2003, **33**, 333.
31 C. Kjølseth, L. Y. Wang, R. Haugsrud, T. Norby, *Solid State Ion.*, 2010, **181**, 1740.
32 D. Han, K. Shinoda, S. Sato, M. Majima, T. Uda, *J. Mater. Chem. A*, 2015, **3**, 1243.
33 H. Takahashi, I. Yashima, K. Amezawa, K. Eguchi, H. Matsumoto, H. Takamura, S. Yamaguchi, *Chem. Mater.*, 2017, **29**, 1518.
34 I. Oikawa, M. Ando, Y. Noda, K. Amezawa, H. Kiyono, T. Shimizu, M. Tansho, H. Maekawa, *Solid State Ion.*, 2011, **192**, 83.
35 Y. Ling, H. Chen, J. Niu, F. Wang, L. Zhao, X. Ou, T. Nakamura, K. Amezawa, *J. Eur. Ceram. Soc.*, 2016, **36**, 3423.
36 Y. Sakuda, J. R. Hester, M. Yashima, *J. Ceram. Soc. Japan*, 2022, **130**, 442.
37 Y. Suzuki, T. Murakami, K. Fujii, J. R. Hester, Y. Yasui, M. Yashima, *Inorg. Chem.*, 2022, **61**, 7537.
38 S. Fop, J. M. S. Skakle, A. C. McLaughlin, P. A. Connor, J. T. S. Irvine, R. I. Smith, E. J. Wildman, *J. Am. Chem. Soc.*, 2016, **138**, 16764.
39 M. Yashima, T. Tsujiguchi, K. Fujii, E. Niwa, S. Nishioka, J. R. Hester, K. Maeda, *J. Mater. Chem. A*, 2019, **7**, 13910.
40 T. Murakami, T. Shibata, Y. Yasui, K. Fujii, J. R. Hester, M. Yashima, *Small*, 2022, **18**, 2106785.
41 Y. Youn, B. Hussain, A. Ullah, I. J. Hwang, J. Shin, J. Hong, D. W. Joh, S. Lee, R. Song, S. Park, T. W. Kim, Y. Choi, T. Lim, H. Kim, *Chem. Mater.*, 2023, **35**, 9493.
42 J. Xu, Q. Cao, L. Wang, B. Ouyang, T. Wei, J. Hao, J. Chen, L. He, L. Liu, K. Huang, *Energy Adv.*, 2024, https://doi.org/10.1039/D3YA00268C.
43 S. Fop, J. A. Dawson, D. N. Tawse, M. G. Skellern, M. S. Jan, A. C. Mclaughlin, *Chem. Mater.*, 2022, **34**, 8190.
44 Y. Yasui, M. Tansho, K. Fujii, Y. Sakuda, A. Goto, S. Ohki, Y. Mogami, T. Iijima, S. Kobayashi, S. Kawaguchi, K. Osaka, K. Ikeda, T. Otomo, M. Yashima, *Nat. Commun.*, 2023, **14**, 2337.
45 T. Murakami, J. R. Hester, M. Yashima, *J. Am. Chem. Soc.*, 2020, **142**, 11653.
46 T. Murakami, M. Avdeev, R. Morikawa, J. R. Hester, M. Yashima, *Adv. Func. Mater.*, 2023, **33**, 2206777.
47 Y. Sakuda, T. Murakami, M. Avdeev, K. Fujii, Y. Yasui, J. R. Hester, M. Hagihala, Y. Ikeda, Y. Nambu, M. Yashima, *Chem. Mater.*, 2023, **35**, 9774.
48 C. A. Fuller, D. A. Blom, T. Vogt, I. R. Evans, J. S. O. Evans, *J. Am. Chem. Soc.*, 2021, **144**, 615.
49 K. Saito, K. Fujii, M. Yashima, *J. Solid State Chem.*, 2022, **306**, 122733.
50 R. Morikawa, T. Murakami, K. Fujii, Y. Nambu, M. Yashima, *Commun. Mater.*, 2023, **4**, 42.
51 M. Yashima, D. Ishimura, *Chem. Phys. Lett.*, 2003, **378**, 395.
52 A. Magrasó, *J. Power Sources*, 2013, **240**, 583.
53 L. Kalland, A. Magraso, A. Mancini, C. Tealdi, L. Malavasi, *Chem. Mater.*, 2013, **25**, 2378–2384.
54 Z. Luo, Y. Zhou, X. Hu, W. Wang, Y. Ding, W. Zhang, T. Li, N. Kane, Z. Liu, M. Liu, *Small*, 2023, **19**, 2208064.
55 R. Oishi, M. Yonemura, Y. Nishimaki, S. Torii, A. Hoshikawa, T. Ishigaki, T. Morishima, K. Mori, T. Kamiyama, *Nucl. Instruments Methods Phys. Res. Sect. A Accel. Spectrometers, Detect. Assoc. Equip.*, 2009, **600**, 94.
56 M. Yonemura, K. Mori, T. Kamiyama, T. Fukunaga, S. Torii, M. Nagao, Y. Ishikawa, Y. Onodera, D. S. Adipranoto, H. Arai, Y. Uchimoto, Z. Ogumi, *J. Phys. Conf. Ser.*, 2014, **502**, 012053.

57 H. Chen, L. L. Wong, S. Adams, *Acta Crystallogr., Sect. B: Struct. Sci.*, 2019, **75**, 18.
58 L. L. Wong, K. C. Phuah, R. Dai, H. Chen, W. S. Chew, S. Adams, *Chem. Mater.*, 2021, **33**, 625.
59 G. Kresse, D. Joubert, *Phys. Rev. B*, 1999, **59**, 1758.
60 A. Stukowski, *Model. Simul. Mater. Sci. Eng.*, 2010, **18**, 015012.
61 K. Momma, F. Izumi, *J. Appl. Crystallogr.*, 2011, **44**, 1272.
62 A. S. Nowick, A. V. Vaysleyb, *Solid State Ion.*, 1997, **97**, 17.
63 T. Norby, *Solid State Ion.*, 1999, **125**, 1.
64 D. Han, N. Hatada, T. Uda, *J. Am. Ceram. Soc.*, 2016, **99**, 3745.
65 J. Hyodo, K. Kitabayashi, K. Hoshino, Y. Okuyama, Y. Yamazaki, *Adv. Energy Mater.*, 2020, **10**, 2000213.
66 K. D. Kreuer, S. Adams, W. Münch, A. Fuchs, U. Klock, J. Maier, *Solid State Ion.*, 2001, **145**, 295.
67 K. D. Kreuer, *Solid State Ion.*, 1999, **125**, 285.
68 R. B. Cervera, S. Miyoshi, Y. Oyama, Y. E. Elammari, T. Yagi, S. Yamaguchi, *Chem. Mater.*, 2013, **25**, 1483.
69 J. Lagaeva, D. Medvedev, A. Demin, P. Tsiakaras, *J. Power Sources*, 2015, **278**, 436–444.
70 S. Choi, C. J. Kucharczyk, Y. Liang, X. Zhang, I. Takeuchi, H. Ji, S. M. Haile, *Nat. Energy*, 2018, **3**, 202–210.
71 I. D. Brown, D. Altermatt, *Acta Crystallogr., Sect. B: Struct. Sci.* 1985, **41**, 244.
72 I. D. Brown, The Chemical Bond In Inorganic Chemistry, Oxford University Press, Oxford, 2002.
73 J. Hyodo, K. Tsujikawa, M. Shiga, Y. Okuyama, Y. Yamazaki, *ACS Energy Lett.*, 2021, **6**, 2985.
74 A. K. E. Andersson, S. M. Selbach, C. S. Knee, T. Grande, *J. Am. Ceram. Soc.*, 2014, **97**, 2654.